

Rate-Limiting Step in Batteries with Metal Oxides as the Energy Materials

Qiang Wang,[†] Mingchao Shang,[†] Yong Zhang,[‡] Yuan Yang,[§] and Yan Wang^{*,†}

[†]Materials Science & Engineering, Worcester Polytechnic Institute, 100 Institute Road, Worcester, Massachusetts 01609, United States

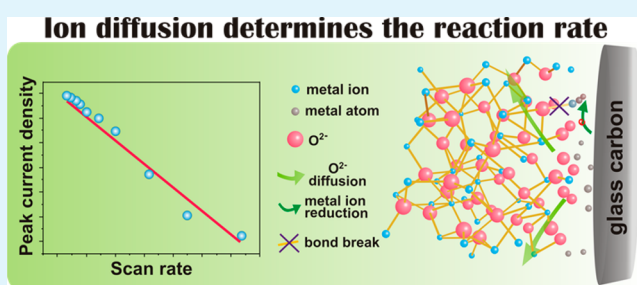
[‡]Center for Materials Science and Engineering, Massachusetts Institute of Technology, 77 Massachusetts Avenue, Cambridge, Massachusetts 02139, United States

[§]Materials Science & Engineering, Columbia University, 200 S.W. Mudd, New York, New York 10027, United States

Supporting Information

ABSTRACT: Metal oxides are used as the energy materials in some aqueous and nonaqueous batteries. However, a large overpotential and poor rate-performance limit their wide application. Low electrical conductivity of the oxide is commonly considered to be the reason for these limitations. The present study specifically reveals the electrochemical reduction process of α -Fe₂O₃ particles by using a cyclic voltammetry technique combined with an electron spectroscopy technique. SEM and TEM observe the phase and crystal structure transformation process during α -Fe₂O₃ reduction at the nanoscale, and EDS analyzes the composition change of particles at various periods. The surface of α -Fe₂O₃ particles is reduced to an amorphous compound first, and then O²⁻ ions diffuse from the crystal matrix toward the outside simultaneously causing defects inside the particles. Experiments prove that γ -Fe₂O₃, Fe₃O₄, CuO, and Bi₂O₃ have the same rate-limiting step as α -Fe₂O₃; that is, O²⁻ ions diffuse inside the oxide particles toward the outside. The diffusion coefficients of O²⁻ in these metal oxides are also estimated. This study demonstrates that the ionic conductivity of metal oxides is the critical factor which affects the overpotential and rate-performance of the batteries with these oxides as active material, and the O²⁻ ion diffusion coefficient must be considered when selecting or designing metal oxides as energy material. The conclusion that O²⁻ diffusion in oxides is the rate-limiting step of their reduction may be applicable to a group of oxides whose reduction reaction is not involved in ion diffusion from an electrolyte into their crystal matrix.

KEYWORDS: metal oxides, O²⁻ ions diffusion, rate-limiting step, diffusion coefficient, defects



INTRODUCTION

Electrochemical reduction of metal oxides is a critical solid-state reaction because it relates to the charge/discharge of primary¹ and secondary batteries,^{2–11} supercapacitors,^{12–15} and electrolysis of metal oxides for metal production.^{16,17} According to the reaction mechanism of the oxides reduction in Li⁺-containing nonaqueous electrolytes, the metal oxides can be classified into three groups:⁸ (1) The first group has the Li⁺ intercalation reaction in their reduction, such as TiO₂, V₂O₅, and MoO₂.¹⁸ (2) The second group has the conversion reaction in their reduction, such as CoO, NiO, CuO,¹⁹ SnO. (3) The third group has intercalation reaction first, followed by the conversion reaction, such as RuO₂, Co₃O₄,²⁰ MnO₂.²¹ However, in aqueous electrolytes, the reduction mechanism of metal oxides is not as clear as it is in nonaqueous electrolytes. For example, the reduction process of iron oxides in alkaline aqueous electrolytes is still ambiguous even though it has been studied for several decades: Sato proposed that Fe₂O₃ was reduced to lower valence oxide in 1970.²² Patrik verified that Fe₂O₃ was reduced to Fe₃O₄ then to Fe(OH)₂ with in situ X-

ray absorption near-edge spectroscopy.²³ However, some scientists still believe that Fe₂O₃ is directly reduced to Fe(OH)₂ at the first stage.^{24,25} Allanore believes that the reaction occurs in solid-state reaction mode, but dissolved species (such as Fe(OH)₃⁻) may also be involved in the reduction.^{26,27} Fe₃O₄ was the intermediate supported by Mossbauer spectra in his studies. Liu believes that the Fe₂O₃ particle reduction rate is controlled by the diffusion step,²⁸ and the diffusing species inside the Fe₂O₃ and Fe₃O₄ crystal matrix was postulated to be H⁺ by other scientists.²⁹ Switzer thinks either the solid-state reaction mode or dissolution/redeposition mode, or both, could happen in the Fe₃O₄ reduction reaction, and the O²⁻ ion was proposed to be the diffusing species inside the crystal matrix in the solid-state reaction mode.³⁰ The understanding of CuO reduction is even more inadequate, and whether CuO is reduced in one step or two steps has been debated for several

Received: December 23, 2017

Accepted: February 5, 2018

Published: February 5, 2018

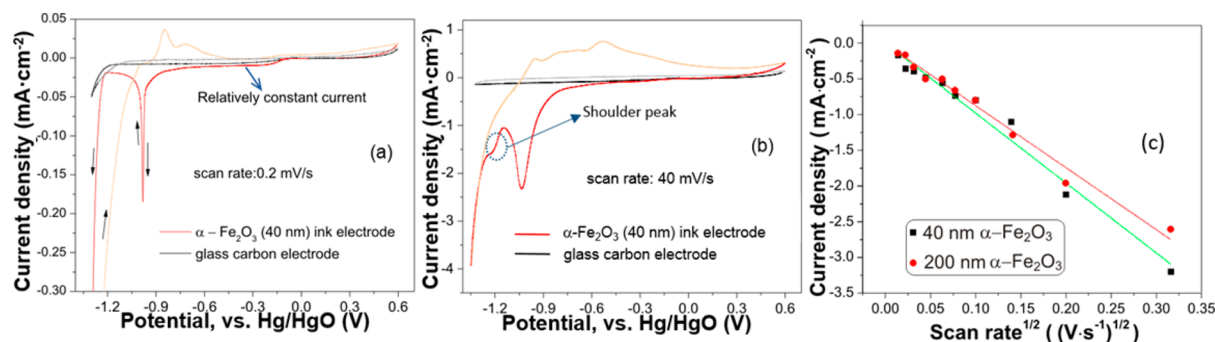
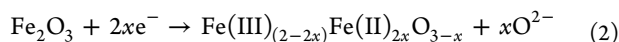
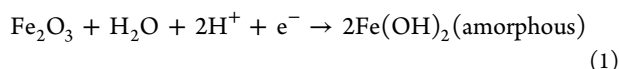


Figure 1. CV profiles with different scan rate and the relationship between their peak current density and the scan rate. (a) CV profile comparison between α -Fe₂O₃ (40 nm) ink electrode and glass carbon electrode, at scan rate of 0.2 mV/s. (b) CV profile comparison between α -Fe₂O₃ (40 nm) ink electrode and glass carbon electrode, at scan rate of 40 mV/s. (c) Relationship between peak current density [i_p (Fe³⁺ to Fe²⁺)] and scan rate (v) in the CV profile of α -Fe₂O₃ ink electrode, with 40 and 500 nm α -Fe₂O₃ particles.

decades.^{1,31–35} Both sides are still presenting new evidence to support their opinions, and this discrepancy cannot be clarified until the reaction process of CuO reduction is well-understood.

In the present study, a group of metal oxides, which include α -Fe₂O₃, γ -Fe₂O₃, Fe₃O₄, CuO, and Bi₂O₃, was determined to have the same rate-limiting step in their electrochemical reductions in the alkaline aqueous electrolyte. For this study, an ink electrode was used for two reasons: First, it can easily track the morphology change of the nanoparticles on the surface of glass carbon at a series of electrode potentials with SEM. Second, the quantity of the metal oxides can be precisely controlled on the electrode surface, and the electrode process kinetics can be analyzed with cyclic voltammetry (CV). TEM/EDS is utilized to analyze the crystal structure and composition changes inside particles at the nanoscale. Two pathways for Fe₂O₃ reduction are presented in the current work. The surface of the particles is reduced to amorphous Fe(OH)₂ first, and then O²⁻ diffuses outward from the interior of the particle as the reduction reaction continues, as shown in eqs 1 and 2. The reduction reaction rate is determined by the O²⁻ diffusion step.



Our experiments prove that α -Fe₂O₃, γ -Fe₂O₃, Fe₃O₄, CuO, and Bi₂O₃ have the same rate-limiting step of O²⁻ diffusion. The O²⁻ ion diffusion coefficient inside these oxides is estimated according to the semi-infinite diffusion equation.

It is well-known that H⁺ diffusion from electrolyte into crystal matrix is the rate-limiting step of RuO₂³⁶ and MnO₂³⁷ reduction in aqueous electrolytes. Herein, a different reaction mechanism is revealed by examining five metal oxides and this mechanism may be applicable to other metal oxides, whose reduction does not involve H⁺ diffusion into the crystal structure of the particle, or reduction from metal oxide to metal directly. This fundamental discovery can provide new insights to improve the low rate-performance and large overpotential of battery charging/discharging; help to select and design metal oxides as energy material in batteries; and elucidate the influence of particle size on their charging/discharging performance.

EXPERIMENTAL SECTION

Preparation of Ink Electrodes. The preparation steps of α -Fe₂O₃ (200 nm, Sigma-Aldrich, purity $\geq 99\%$), α -Fe₂O₃ (~ 30 – 40 nm, Alfa

Aesar), γ -Fe₂O₃ (~ 30 – 40 nm, Alfa Aesar), Fe₃O₄ (~ 20 – 30 nm, Alfa Aesar), CuO (~ 30 – 50 nm, Alfa Aesar), and Bi₂O₃ (~ 30 – 40 nm, Alfa Aesar) ink electrodes were as follows: A 50 mg portion of oxide was dispersed in 5 mL of Nafion solution (0.05 wt % Nafion solution with ethanol as solvent) with ultrasonic vibration for 1 h. By using a microsyringe pipet, 5 μ L of the suspension was dropped to the surface of a glass carbon electrode (diameter 5 mm). The ethanol was vaporized by putting the electrode under an infrared lamp, and oxide was firmly bonded on the surface of the glass carbon.

Electrochemical Test. A four-neck electrolyte cell with vacuum sealing was employed for the CV test. The auxiliary electrode was Pt wire, and all the potentials were measured with Hg/HgO electrode as reference. Electrolyte was prepared by dissolving KOH pellets (VWR, ACS grade) into pure water (Fisher scientific, HPLC grade) with 20 wt % KOH inside. Nitrogen gas was purged inside the cell, and the gas outlet was sealed with mineral oil to keep good nitrogen atmosphere inside the cell. Nitrogen gas was purged inside the cell for 20 min each time before electrochemical test. A Luggin capillary was inserted to the surface of the working electrode as closely as possible to avoid any ionic IR drop inside the electrolyte. The electrolyte on glass carbon surface was static during the test, and each ink electrode was just scanned one cycle.

SEM Characterization. A JSM-7000F instrument was used for SEM. After the potentiodynamic polarization, the electrode head was unscrewed from the stem inside glovebox and was transferred into the SEM for analysis.

STEM/TEM Characterization. After each session of LSV test, the ink electrode was ultrasonicated in 1 mL of anaerobic ethanol to remove particles from the glass carbon, dispersing them into the ethanol. The suspension was decanted by glass pipet, and dropped onto a copper grid inside the glovebox; then, the copper grid was transferred into TEM under Ar atmosphere. A JEOL JEM 2010F microscope was used to characterize the sample with a gun voltage of 200 kV.

RESULTS AND DISCUSSION

Electrochemical Reduction Process of α -Fe₂O₃ and Its Reaction Kinetics. Three CV curves from different α -Fe₂O₃ ink electrodes were very similar, as shown in Figure S1, and the repeatability demonstrated that the ink electrode was a reliable tool for the study of metal oxide reduction kinetics. The ink electrodes were scanned from open circuit potential (OCP) to ~ -1.3 V (versus Hg/HgO), then scanned back to 0.6 V (versus Hg/HgO), and scanned to OCP again. The goal of this work is to study the reduction of metal oxides, so the main focus is on the current as the potential was decreased from the right to the left side in the CV profile. Figure 1a compares a typical CV curve of an α -Fe₂O₃ (Alfa Aesar, 40 nm) ink electrode to a typical CV curve of the glass carbon electrode at

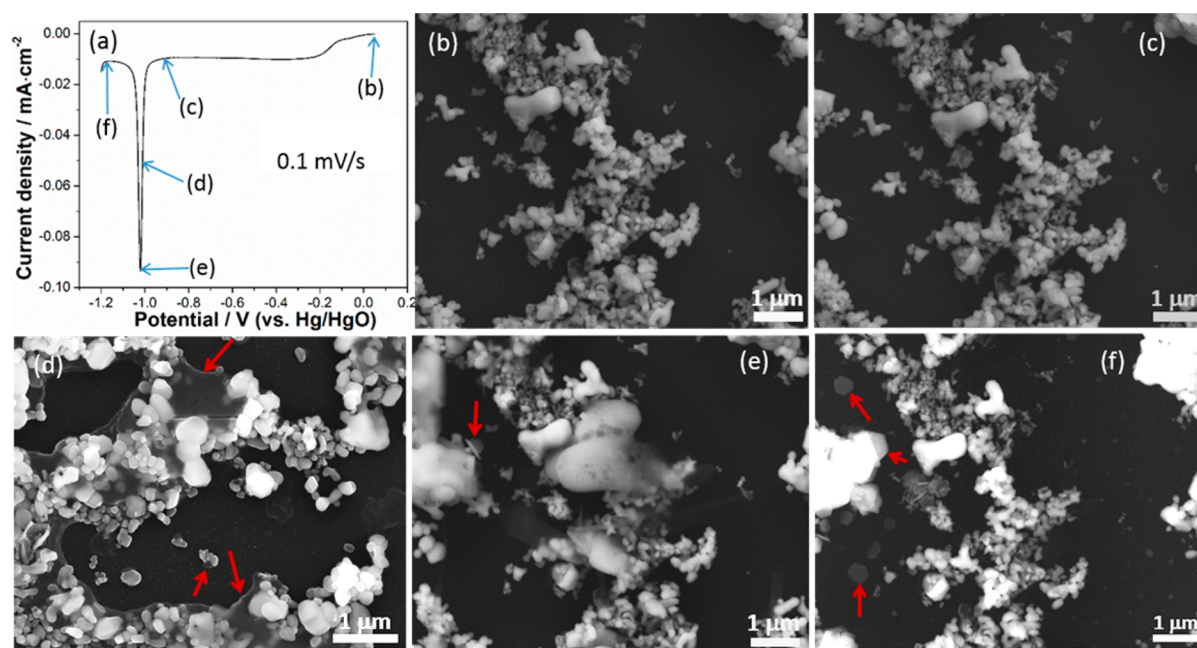
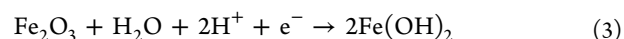


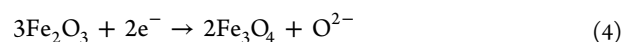
Figure 2. Morphology change of α -Fe₂O₃ ink electrode after potential scanning to different values. (a) LSV test for α -Fe₂O₃ ink electrode. The electrode potential scan was stopped in positions b–f for SEM analysis. (b) Morphology of α -Fe₂O₃ ink electrode before LSV test. (c) Morphology of α -Fe₂O₃ ink electrode after potential scanned to point c. (d) Morphology of α -Fe₂O₃ ink electrode after potential scanned to point d. The arrows in the image point to amorphous compound collapsing from the particles. (e) Morphology of α -Fe₂O₃ ink electrode after potential scanned to point e. Hexagonal flakes begin to form at this point, as the arrow indicates. (f) Morphology of α -Fe₂O₃ ink electrode after potential scanned to point f. All of the amorphous compound were converted into the hexagonal flakes at the potential of point f.

a scan rate of 0.2 mV/s. For the glass carbon electrode, the current only came from electric double layer (EDL) capacitance from 0.6 V (versus Hg/HgO) to OCP, and the current came from both EDL capacitance and the reduction of residual O₂ in electrolyte from OCP to −1.2 V (versus Hg/HgO). For the Fe₂O₃ ink electrode, the current from 0.6 V (versus Hg/HgO) to OCP was mainly from EDL capacitance, and the cathodic current from OCP to −1.2 V (versus Hg/HgO) was from EDL capacitance, residual O₂ reduction, and Fe₂O₃ reduction. Some H₂ gas was also evolved on both of the electrodes when the potential was below −1.2 V (versus Hg/HgO). The overlapping of the two cathodic currents of the two electrodes from 0.6 V (versus Hg/HgO) to OCP demonstrates that the EDL capacitances of these two electrodes were very close to each other, and the residual O₂ reduction currents from these two electrode should also be very close. Therefore, the difference between the currents of the two electrodes from OCP to −1.2 V (versus Hg/HgO) was due to Fe₂O₃ reduction. Figure 1a shows that the reduction of Fe₂O₃ starts from OCP [at \sim −0.1 V (versus Hg/HgO)], and the reaction rate increased gradually from OCP to −0.24 V (versus Hg/HgO). Then, it keeps a relatively constant value from −0.24 V (versus Hg/HgO) to \sim −0.7 V (versus Hg/HgO). There is a reduction peak from \sim −0.7 V (versus Hg/HgO) to −1.2 V (versus Hg/HgO), and the peak was commonly attributed to reduction of Fe(III) to Fe(II).^{17,38} The cathodic current increases dramatically when the potential was less than −1.2 V (versus Hg/HgO), and it was considered to represent both the reduction of Fe(III) and Fe(II) to Fe and H₂ evolution.¹⁷ It is noteworthy that the shape of CV profile depends on the scan rate, and Figure 1b shows that the CV profile (Alfa Aesar, 40 nm) at scan rate of 40 mV/s has a broad reduction peak representing the reduction of Fe(III) to Fe(II), and a new shoulder peak. α -Fe₂O₃ particles with 40 and 200 nm particle size were studied by CV at a series

of scan rates. (A new electrode was used for only one scan rate in the CV profiles shown in the Supporting Information.) All the peak current densities [i_p (Fe(III) to Fe(II))] in those CV profiles were proportional to the square root of the scan rate ($\sqrt{\nu}$), as shown in Figure 1c. The background current (including the current from residual O₂ reduction and EDL capacitance) was subtracted from i_p (the detailed method is described in Figure S4). The relationship of current density and scan rate shows that an unknown ion diffusion inside the crystal matrix of the particle was the rate-limiting step^{15,28,39} because the ion diffusion coefficient in solution was several orders higher than the same ion diffusion coefficient inside a crystal matrix. For example, the diffusion coefficient of H⁺ in aqueous solution is 9.34×10^{-5} cm²/s, but it is only 3.1×10^{-10} cm²/s inside Ni(OH)₂ particles.³⁸ If Fe(OH)₂ was the intermediate for α -Fe₂O₃ reduction,^{24,25} as eq 3 shows, both H⁺ and H₂O species should diffuse from electrolyte into the crystal matrix of Fe₂O₃ particle, and their diffusion determines the rate-limiting step.



However, if Fe₃O₄ was the intermediate,^{23,26,27} as eq 4 shows, then O^{2−} ions diffuse from the crystal matrix of Fe₂O₃ particles into electrolyte, and the diffusion determines the rate-limiting step.



For clarification of the reaction mechanism, SEM and HR-TEM combined with EDS analysis were utilized to give a detailed and specific description of the reaction process at the nanoscale. The knowledge of the phase transformation inside crystal matrix during the reaction was very helpful to understand the

reaction process and determine what kind of ions diffuse inside the particles.

For easy observation of the morphology change during the reduction process with SEM, large Fe_2O_3 particles (~ 200 nm) were selected for the potentiodynamic polarization. As shown in Figure 2a, the Fe_2O_3 ink electrode was scanned at 0.1 mV/s from OCP to -1.2 V (versus Hg/HgO) in a KOH solution; when the potential reached point c [-0.9 V (versus Hg/HgO)], point d [-1.0 V (versus Hg/HgO)], point e [-1.01 V (versus Hg/HgO)], and point f [-1.2 V (versus Hg/HgO)], the scanning was stopped for SEM analysis. After pulling out from electrolytic cell, the electrode was washed with deoxygenized ethanol three times to avoid interference from the solid KOH, and then was transferred into the SEM for morphology analysis under N_2 protection. Each Fe_2O_3 particle on the glass carbon surface can be clearly observed, with particle sizes from 80 nm to 1 μm before the linear scanning voltammetry (LSV) test, as shown in Figure 2b. It took 2.5 h for the dynamic potential to polarize from OCP to -0.9 V (versus Hg/HgO), but Figure 2c shows that the number and the morphology of the particles were not changed from the scanning process. The same morphology and quantity of the particles demonstrate that Fe_2O_3 particles were not dissolved into the electrolyte during the early stage of LSV, even though the solubility of Fe_2O_3 was reported to be 1×10^{-4} mol/L in 20 wt % KOH solution at 303 K.⁴⁰ Activation energy needs to be overcome for Fe_2O_3 particle dissolution, and a common way to dissolve solid particles is to heat or stir the solution. The solubility reported previously was obtained after stirring Fe_2O_3 particles inside KOH solution for several hours.⁴⁰ In the present study, the LSV test was carried out at room temperature in static electrolyte, and no Fe_2O_3 particle dissolved into the electrolyte directly. All the particles at the different potential points were also analyzed with TEM to observe the crystal structure transformation. As the HR-TEM image of Figure 3b shows, an amorphous shell coated on the Fe_2O_3 particle as the potential was scanned from point b to c, and this proves that the cathodic current from OCP to -0.9 V (versus Hg/HgO) corresponded to the reduction of the surface of the Fe_2O_3 particle to amorphous shell. When the electrode potential was polarized to more negative values, the thickness of the shell increased gradually, and Figure 2d shows that the amorphous compound collapsed from the particle surface onto the glass carbon, as the arrows indicate, when the electrode potential was at point d. At the peak potential, the amorphous compound coalesced and reached its maximum size. This coalescence verified that the amorphous compound followed a dissolution/redeposition process.^{26,27} At the same time, a new crystal phase with hexagonally shaped flakes started to appear on the surface of the glass carbon, as the arrow indicates. When the electrode potential polarized to -1.20 V (versus Hg/HgO), all the amorphous compound was converted into the hexagonal crystalline flakes, as shown in Figure 2f. The electron diffraction pattern in Figure S7 shows that these flakes are crystal $\text{Fe}(\text{OH})_2$. By comparing Figure 2b and Figure 2f, another phenomenon can be observed: some particles kept their original shape and size; some became smaller, and some disappeared. The particles at points b, d, and f were compared with TEM analysis, and Figure 3 clearly demonstrates that the crystal structure changes inside the particles. Figure 3a shows that the Fe_2O_3 particle before LSV had a perfect crystal structure with a prominent crystal lattice. The particle at -0.9 V (versus Hg/HgO) in Figure 3b has the similarly prominent

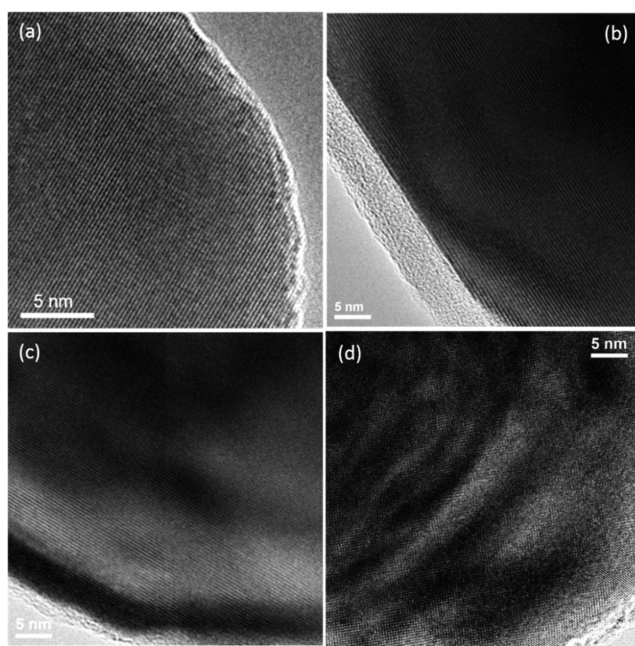


Figure 3. Microstructure of $\alpha\text{-Fe}_2\text{O}_3$ particles scanned to different electrode potential. (a) Particle before LSV test. (b) Particle scanned to -0.9 V (vs Hg/HgO). (c) Particle scanned to -1.012 V (vs Hg/HgO). (d) Particle scanned to -1.2 V (vs Hg/HgO).

crystal lattice with some indistinct crystal defects. At the peak potential of point e, the crystal defects inside the particle became very obvious, and at -1.2 V (versus Hg/HgO) there were even more crystal defects appearing inside the crystal particle (see the contrast change inside the particles in Figure 3d), which is associated with the relaxation of stress during phase conversion. The corresponding TEM images of the integral particles are shown in Figure S8. These TEM images verify that some ions diffused from the crystal matrix outward, or diffused from electrolyte into the crystal matrix to form defects in the particles, and this phenomenon was consistent with the relationship of the current density and scan rate in Figure 1c. EDS was utilized to identify the amorphous shell outside and the defects inside the particle. Figure 4a shows the particle with the amorphous shell after being scanned to point c, and the Fe/O atom ratios of the shell and the different parts

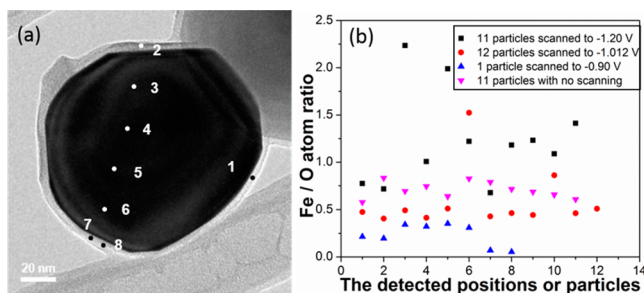


Figure 4. EDS detecting position of partially reduced Fe_2O_3 , and the corresponding Fe/O ratio of particles at different potential. (a) The 8 positions of EDS point detected on Fe_2O_3 particle scanned to -0.9 V; the 1st, 2nd, 7th, and 8th tests were on the amorphous shell, and the 3rd, 4th, 5th, and 6th tests were on the crystal structure of the Fe_2O_3 particle. (b) Fe/O atom ratios of the different parts of an Fe_2O_3 particle scanned to -0.9 V, or the Fe/O atom ratio of different particles scanned to different potential positions.

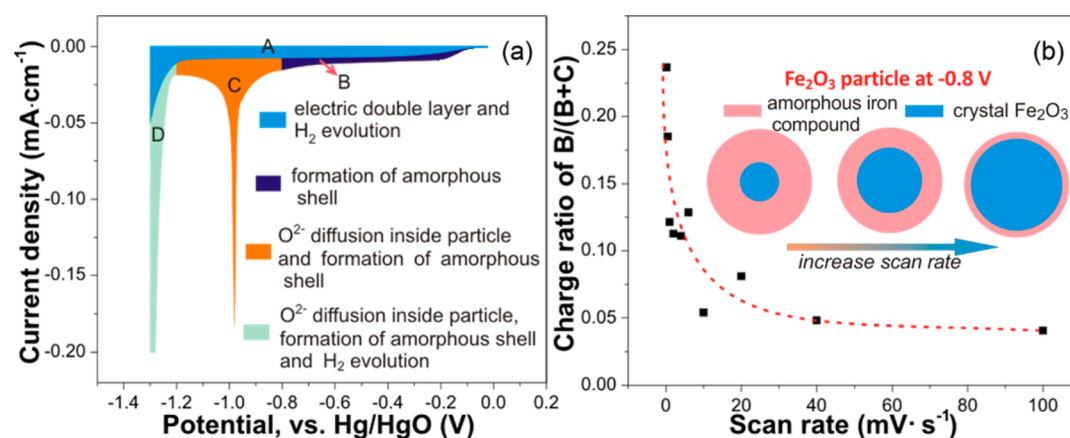


Figure 5. Estimation of the thickness of $\text{Fe}(\text{OH})_{2/\text{amor}}$ shell coating on Fe_2O_3 particle at -0.8 V (vs Hg/HgO). (a) Partition of the charge consumed in LSV test of $\alpha\text{-Fe}_2\text{O}_3$ ink electrode from OCP to -1.3 V (vs Hg/HgO). (b) Ratio of charge for $\text{Fe}(\text{OH})_{2/\text{amor}}$ shell formation to the total charge for both $\text{Fe}(\text{OH})_{2/\text{amor}}$ shell formation and O^{2-} diffusion at different scan rates.

inside the particle were analyzed by EDS point detection. The results are shown in Figure 4b, which demonstrate the very close values from points 3, 4, 5, and 6, and this means that the Fe/O atom ratio was very constant inside the particle. The detecting points 1, 2, 7, and 8 were on the amorphous shell, and these points had relatively lower Fe/O atom ratio than that of points 3, 4, 5, and 6. Because the amorphous iron compound was eventually transformed into crystal $\text{Fe}(\text{OH})_2$ under a lower potential polarization, it can be considered to be amorphous $\text{Fe}(\text{OH})_2$ ($\text{Fe}(\text{OH})_{2/\text{amor}}$), which has a lower Fe/O atom ratio than crystal Fe_2O_3 , and is consistent with the ratio determined by the EDS point analysis. More than 10 particles were randomly selected at each potential of points b, e, and f for EDS point analysis, and the detection position was close to the center of each particle. Figure 4b demonstrates that the Fe/O atom ratio was determined by the ending potential, and provides the general order as -0.9 V < -1.012 V < OCP < -1.2 V, even though two particles with the ending potential of -1.012 V (versus Hg/HgO) had higher Fe/O atom ratio than the other particles at OCP and some particles with the ending potential of -1.2 V (versus Hg/HgO). These two particles were much smaller, causing a more complete reaction and relatively high Fe/O atom ratio. At OCP, 11 Fe_2O_3 particles had Fe/O atom ratio near the theoretical value of 0.667. The particle scanned to -0.9 V (versus Hg/HgO) and the particles scanned to -1.012 V (versus Hg/HgO) have the Fe/O atom ratios lower than the ratios of the Fe_2O_3 particles at OCP. The lower values are due to the formation of the $\text{Fe}(\text{OH})_{2/\text{amor}}$ shell, which coated the particles, because the electron beam from the TEM gun passed through two $\text{Fe}(\text{OH})_{2/\text{amor}}$ layers and the interior of the crystal Fe_2O_3 before the electrons were analyzed by the instrument, and the Fe/O atom ratio from these particles was the average value from the two phases. The Fe/O atom ratios are in the order of -0.9 V < -1.012 V < -1.2 V, and the order firmly verifies that the crystal defects in Figure 3b–d were not caused by H^+ and H_2O diffusion from electrolyte into Fe_2O_3 crystal matrix; otherwise, Fe/O atom ratios would decrease with the electrode potential decreasing. The increase of Fe/O atom ratio can be caused by either O^{2-} ion diffusion from the interior of Fe_2O_3 particles toward the outside, or $\text{Fe}(\text{II})$ ions diffusion from the exterior into the interior of particles. However, the latter situation cannot happen, because when the electrode potential was polarized from OCP to the cathodic peak potential, some of the Fe–O

bonds were broken by the driving force from electrode potential; a part of $\text{Fe}(\text{III})$ ions inside the crystal framework were reduced to $\text{Fe}(\text{II})$ ions, and these $\text{Fe}(\text{II})$ ions were still inside the crystal framework connecting with the O^{2-} ion. However, a part of the O^{2-} ions can become isolated from the crystal framework, and they diffused from crystal matrix into electrolyte.

The electrochemical reduction of Fe_2O_3 particles employs two pathways as shown by the above experiments: the surface of Fe_2O_3 particles was reduced to $\text{Fe}(\text{OH})_{2/\text{amor}}$ at the early stage, and when the electrode potential was lower than a certain value, then O^{2-} ions inside the particles started to diffuse toward the outside simultaneously with the continuous formation of $\text{Fe}(\text{OH})_{2/\text{amor}}$ outside the particle. O^{2-} diffusion was the rate-limiting step in this reduction process. Comparison of the reduction charge in different potential regions can enable the determination of the dominant pathway. Excluding the charge from EDL capacitance, the reduction charge can be divided into three parts: the charge for reducing the surface of Fe_2O_3 particle forming $\text{Fe}(\text{OH})_{2/\text{amor}}$, the charge for reducing the internal part of Fe_2O_3 particle introducing O^{2-} defects inside the particles, and the charge for evolving H_2 gas. The LSV curve of Fe_2O_3 ink electrode reduction was integrated from OCP to -1.2 V (versus Hg/HgO), and the integral was divided by the scan rate to correspond to the total charge, including both faradic and nonfaradic charge. The same procedure was applied to the LSV data from the glass carbon electrode, and the result corresponds to the charge from EDL capacitance and residual O_2 reduction. The charge for Fe_2O_3 reduction can be obtained by subtracting the charge of EDL capacitance and residual O_2 reduction from the total charge, and this Fe_2O_3 reduction charge was approximately divided into two parts. The first part is from OCP to the ~ -0.8 V region, which roughly corresponded to the formation of $\text{Fe}(\text{OH})_{2/\text{amor}}$ shell and is marked as letter B in Figure 5a; the second part is from ~ -0.8 V (versus Hg/HgO) to ~ -1.2 V (versus Hg/HgO), which corresponds to the formation of both $\text{Fe}(\text{OH})_{2/\text{amor}}$ shell and O^{2-} defects inside Fe_2O_3 particles, and is marked as letter C in Figure 5a. The value of $B/(B + C)$ reflected the contribution of the $\text{Fe}(\text{OH})_{2/\text{amor}}$ formation pathway to the total reduction reaction. The value decreased dramatically with increased scan rate, as shown in Figure 5b, and the decrease demonstrates that the thickness of the $\text{Fe}(\text{OH})_{2/\text{amor}}$ shell coating on the particle became thinner as

the scan rate in the OCP to -0.8 V (versus Hg/HgO) region increased. This explanation is consistent with the TEM analysis shown in Figure S9. Because the amorphous compound can collapse onto glass carbon as Figure 2d shows, the average distance of O^{2-} ion diffusion inside particles became longer with increased scan rate. This diffusion distance was directly related to the overpotential for oxide reduction. When the ion diffusion distance is longer, the overpotential is larger, and the CV peak is broader. Seung's group reported that the strength of Mo–O bond in the MoO_2 particle depends on particle size,⁸ and Joachim's group reported that grain size of NiO influences its overpotential.⁴¹ Both reported phenomena can be attributed to the influence of the O^{2-} diffusion distance on the reduction overpotential. When the CV test was conducted for $\alpha\text{-Fe}_2\text{O}_3$ (40 nm) ink electrode at a very low scan rate of 0.2 mV/s, as shown in Figure 1a, a very large part of Fe_2O_3 from each particle participated in the reaction pathway of forming $Fe(OH)_{2/amar}$, leading to a very short O^{2-} ion diffusion distance and a very small overpotential for Fe_2O_3 reduction. Therefore, the width of the reduction peak ($Fe(III)$ to $Fe(II)$) was very narrow. As a comparison, the CV test conducted for a similar $\alpha\text{-Fe}_2\text{O}_3$ (40 nm) ink electrode at a scan rate of 40 mV/s had a much broader reduction peak, as shown in Figure 1b. The shoulder peak in Figure 1b was also caused by the limited diffusion rate of O^{2-} ions inside of the particles. The time for O^{2-} diffusion inside the particles became short at high scan rates. The reduction of some $Fe(III)$ ions, which could be reduced at ~ -1.012 V (versus Hg/HgO) at 0.2 mV/s, was delayed to ~ -1.2 V (versus Hg/HgO) at 40 mV/s due to a longer diffusion distance and a shorter diffusion time. This is the reason that the shoulder peak appeared only at a high scan rate.

Reaction Kinetics of CuO's Electrochemical Reduction. It can be applied to other metal oxides that O^{2-} diffusion is the rate-limiting step in the electrochemical reduction of oxide. In the following sections, the rate-limiting step for CuO and Bi_2O_3 reduction is determined. A series of CV tests were conducted for CuO (~ 50 nm particle size) ink electrodes, as shown in Figure S11, and the current density of the cathodic peak was proportional to the square root of the scan rate, as shown in Figure 6a,b. The linear relationship demonstrates that ion diffusion inside particles was the rate-limiting step. When the electrode was scanned to the cathodic peak potential, CuO particles on the surface electrode were analyzed with TEM. Figure 6c,d shows that the defects were formed inside CuO particles. EDS analysis proved that the Cu/O atom ratio of these particles was higher than the value of 1:1 of the initial CuO particles, and verified that the crystal defects in Figure 6c,d were O^{2-} defects due to O^{2-} diffusion from the crystal matrix outward. Therefore, the rate-limiting step of CuO reduction is O^{2-} ion diffusion. The reduction process which was observed here is consistent with that of Tarascon's report, which showed that the CuO reduction mechanism in nonaqueous electrolyte was involved in the phase transformation from CuO to a solid solution of $Cu^{II}_{1-x}Cu^I_xO_{1-x/2}$ ($0 \leq x \leq 0.4$), to Cu_2O , and to Cu eventually,⁴² but is incompatible with Osakai's studies, which showed that the reduction of CuO occurred in one step, from CuO directly to Cu. Osakai deduced the CuO reduction process by using CV profiles, and the one-step reaction mechanism was supported by the appearance of only one cathodic peak representing the direct reduction from CuO to Cu. However, the series of CV tests in Figure S11 shows that one cathodic peak only appeared

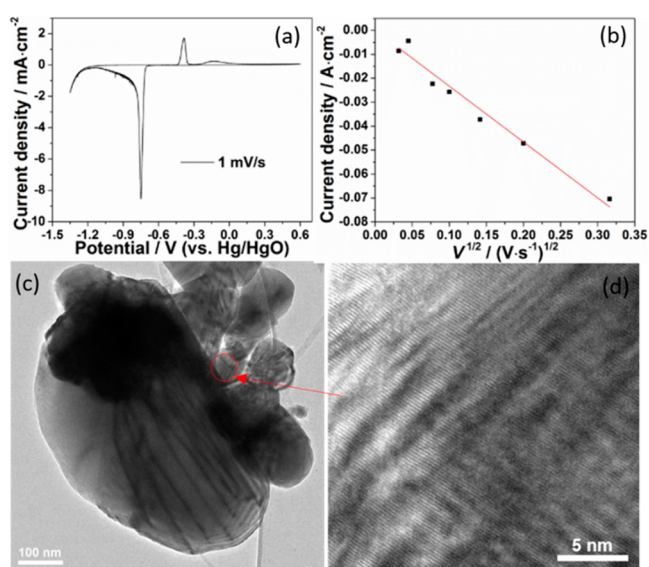


Figure 6. Rate-limiting step of O^{2-} diffusion inside CuO particle during the electrochemical reduction. (a) CV profile of CuO ink electrode. (b) Peak current density and scan rate relationship. The current density is proportional to the square root of scan rate. (c) CuO particles with O^{2-} defects inside. (d) High-magnification TEM image of a CuO particle with O^{2-} defects inside.

at low scan rates, and it can split into two peaks at high scan rates. Our CV tests demonstrate that the O^{2-} diffusion was relatively fast, and the two reduction reactions of CuO to Cu_2O , and Cu_2O to Cu, were hardly separated at low scan rate, but can be separated at high scan rate.

Reaction Kinetics of Bi_2O_3 's Electrochemical Reduction. A series of CV tests was also conducted for Bi_2O_3 (~ 30 nm particle size) ink electrodes, and the current density of the cathodic peak was proportional to the square root of the scan rate, as shown in Figure 7a,b. Figure 7c shows that Bi_2O_3 particles, which were scanned to the peak potential of -0.7 V (versus Hg/HgO), had defects inside the particles, and EDS analysis determined that they were the O^{2-} defects. Therefore, O^{2-} diffusion from inside of particles outward was also the rate-limiting step of Bi_2O_3 reduction. However, there are some differences between the reduction of iron oxides and the oxides of CuO and Bi_2O_3 . During the reduction process of CuO and Bi_2O_3 particles, no amorphous compound formed outside these two oxides. Only a solid solution with defects inside formed initially; then, the particles collapsed to form several smaller particles, as shown in Figure S15a and b. Two more iron oxides ($\gamma\text{-Fe}_2\text{O}_3$ and Fe_3O_4) were studied using CV, and they have the same rate limiting step: O^{2-} diffusion outward from the interior of the crystal matrix controls the whole reduction reaction rate, as shown in the Supporting Information. O^{2-} diffusion inside the crystal matrix of these oxides controls the electrochemical reduction rate; in other words, the ionic conductivity of these oxides is the critical factor determining the rate-performance and the discharging/charging overpotential by using these oxides as energy materials inside batteries, because ion mobility is proportional to the ionic conductivity, as shown in eq 5:

$$\kappa = F \sum_i |z_i| u_i C_i \quad (5)$$

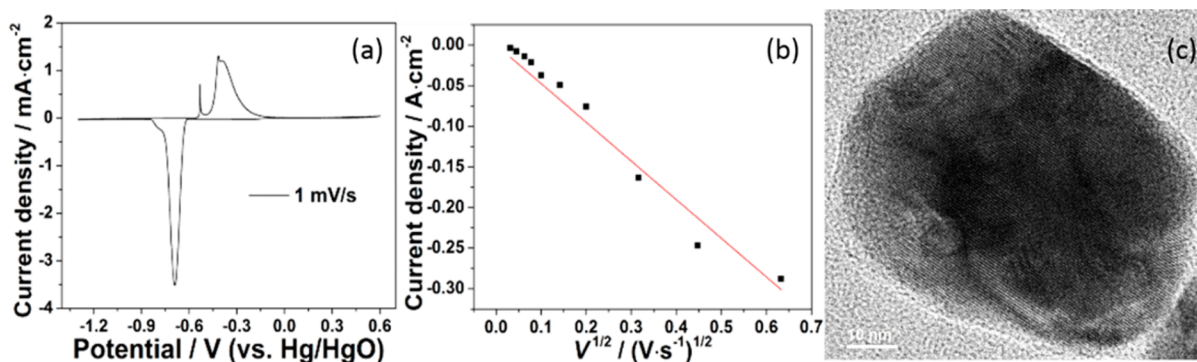


Figure 7. Rate-limiting step of O^{2-} diffusion inside Bi_2O_3 particle during the electrochemical reduction. (a) CV profile of Bi_2O_3 ink electrode. (b) Peak current density and scan rate relationship; the current density is proportional to square root of scan rate. (c) Bi_2O_3 particle with O^{2-} defect inside.

In the equation, u_i is the ion diffusion rate inside the crystal matrix, or the ion mobility; C_i is the ion concentration; z_i is the magnitude of the ion charge.

In addition to the above five metal oxides, the reduction of other metal oxides may be considered to be O^{2-} diffusion outward from the interior of the particle as the rate-limiting step, including the following: (1) ZnO ,⁴³ CdO ,^{44,45} RuO_2 ,⁴⁶ AgO ,⁴⁷ HgO , Au_2O_3 ,⁴⁸ PtO_2 ,⁴⁹ SnO_2 ,⁵⁰ and PbO ,⁵¹ which are reduced from high-valence oxide to low-valence oxide, then to metal, or directly reduced to metal, and have no H^+ ions participating in the reduction reaction when the reduction is carried out in an aqueous electrolyte; (2) some metal oxides, which are reduced to lower valence oxides directly inside alkaline solutions without H^+ ions diffusing into their crystal matrix, but may need H^+ ions for further reduction, such as TiO_3 to TiO_2 , and MoO_3 to MoO_2 ;⁵² and (3) metal oxides such as CuO , CoO , FeO , NiO , MnO ,⁵³ and SnO which are reduced by the conversion reaction in nonaqueous electrolytes containing Li^+ ions. O^{2-} ions diffuse from the interior of the oxides to the outside, combining with Li^+ to form Li_2O .

Estimation of O^{2-} Diffusion Coefficient Inside the Five Metal Oxide Particles. Some studies show H atom diffusion on Pt surfaces⁵⁴ and H^+ ion diffusion inside NiO_2 and MnO_2 particles,^{37,39,55} and include the estimate of the diffusion coefficient.⁵⁶ Here the O^{2-} ion diffusion coefficients in different iron oxides, bismuth oxide, and copper oxide are estimated using the semi-infinite diffusion eq 6, and Note 1 in the Supporting Information gives details. In eq 6, α is the transfer coefficient, A is the real electrode surface area, D is the diffusion coefficient, C_s^0 is the bulk concentration of O^{2-} ions in the crystal matrix of oxides, and ν is the scan rate of the CV test.

$$I_p = (2.99 \times 10^5) \alpha^{1/2} A D^{1/2} C_s^0 \nu^{1/2} \quad (6)$$

The coefficient is on the order of $10^{-13} \text{ cm}^2 \text{ s}$ in $\alpha\text{-Fe}_2\text{O}_3$, $10^{-12} \text{ cm}^2 \text{ s}$ in Fe_3O_4 , $10^{-14} \text{ cm}^2 \text{ s}$ in $\gamma\text{-Fe}_2\text{O}_3$, $10^{-9} \text{ cm}^2 \text{ s}$ in Bi_2O_3 , and $10^{-10} \text{ cm}^2 \text{ s}$ in CuO . Castle reported that the self-diffusion coefficient of oxygen in Fe_3O_4 is $10^{-17} \text{ cm}^2 \text{ s}$ at room temperature, but he also mentioned that water vapor can increase the diffusion coefficient to $10^{-13} \text{ cm}^2 \text{ s}$,⁵⁷ which is very close to the value in the present study. Fe_3O_4 particles piled up on the glass carbon surface, and the pores inside the Fe_3O_4 layer were filled with electrolyte. Therefore, O^{2-} ions do not need to diffuse through the entire layer, and they were released directly into the electrolyte in the pore. This can be the reason why the diffusion coefficient is relatively large in the present study.³⁰

CONCLUSIONS

In this study, we first clarified the electrochemical reduction process of $\alpha\text{-Fe}_2\text{O}_3$, and it involved two parallel pathways. The surface of the particles was reduced to amorphous $\text{Fe}(\text{OH})_2$ in the early stage. With reduction proceeding, this amorphous compound collapses from the surface of the particle, coalesces, and recrystallizes as $\text{Fe}(\text{OH})_2$. Inside the amorphous shell, O^{2-} ions diffuse from the interior of Fe_2O_3 particles outward to form O^{2-} defects, and this diffusion step determines the whole reduction rate. The O^{2-} diffusion step also determines the electrochemical reaction rate of CuO , Bi_2O_3 , $\gamma\text{-Fe}_2\text{O}_3$, and Fe_3O_4 reduction, and O defects form inside these particles during the reaction process. This conclusion, that O^{2-} diffuses outward from the interior of the oxide particles, can probably be applied to metal oxides whose electrochemical reduction process involves no ion diffusion from electrolyte into the crystal matrix of metal oxides. The rule can help to elucidate the influence of particle size on the overpotential of oxide reduction. The bigger particles have longer O^{2-} ion diffusion distances, leading to larger overpotential for the reduction. The O^{2-} diffusion coefficient in the crystal matrix is the critical parameter to select or design metal oxides as energy material of batteries, and the oxides, which have large diffusion coefficient, have low overpotential and high round-trip energy efficiency during their charge/discharge process. One point must be emphasized; that is, the conclusion of O^{2-} diffusion determining the rate-limiting step is based on several layers of particles with particle size larger than 20 nm on the surface of the current collector. For some supercapacitors, a single layer of particles is coated on a current collector with the particle size less than 5 nm, and the rate-limiting step is the surface reaction.

ASSOCIATED CONTENT

Supporting Information

The Supporting Information is available free of charge on the ACS Publications website at DOI: 10.1021/acsami.7b19541.

CV test results, SEM morphology, calibration of the current density of cathodic peak, TEM characterizations, electron diffraction patterns, current density vs scan rate, and estimation of O^{2-} diffusion coefficient (D) (PDF)

AUTHOR INFORMATION

Corresponding Author

*E-mail: yanwang@wpi.edu.

ORCID 

Yuan Yang: 0000-0003-0264-2640

Yan Wang: 0000-0003-1060-2956

Author Contributions

The experiments were designed by Q.W. and Y.W., and conducted by Q.W., M.S., and Y.Z. The results are analyzed by Q.W. and Y.W. The manuscript was written by Q.W., Y.W., Y.Y. Q.W., M.S., Y.Z., Y.Y., and Y.W. have given approval to the final version of the manuscript.

Funding

Funding from Worcester Polytechnic Institute and the MassCEC Catalyst Award is gratefully acknowledged.

Notes

The authors declare no competing financial interest.

ACKNOWLEDGMENTS

We acknowledge the helpful discussion on TEM from Yangyang Fan, the useful language improvement from Roy D. Hegedus, and the supply of TEM instrument from MIT Center for Materials Science and Engineering.

REFERENCES

- (1) Jones, T. W.; Lewandowski, A. P.; Donne, S. W. Discharge Performance of a Primary Alkaline CuO Cathode Material Prepared via a Novel Non-aqueous Precipitation Method. *Electrochim. Acta* **2011**, *56* (14), 4996–5002.
- (2) Liu, J.; Chen, M.; Zhang, L.; Jiang, J.; Yan, J.; Huang, Y.; Lin, J.; Fan, H. J.; Shen, Z. X. A Flexible Alkaline Rechargeable Ni/Fe Battery Based on Graphene Foam/Carbon Nanotubes Hybrid Film. *Nano Lett.* **2014**, *14* (12), 7180–7187.
- (3) Santhoshkumar, P.; Prasanna, K.; Jo, Y. N.; Sivagami, I. N.; Kang, S. H.; Lee, C. W. A Facile and Highly Efficient Short-time Homogenization Hydrothermal Approach for the Smart Production of High-quality Alpha-Fe₂O₃ for Rechargeable Lithium Batteries. *J. Mater. Chem. A* **2017**, *5* (32), 16712–16721.
- (4) Li, J.; Guo, L. T.; Shanguan, E.; Yue, M. Z.; Xu, M.; Wang, D.; Chang, Z. R.; Li, Q. M. Synthesis of Novel Spherical Fe₃O₄@Ni₃S₂ Composite as Improved Anode Material for Rechargeable Nickel-iron Batteries. *Electrochim. Acta* **2017**, *240*, 456–465.
- (5) Wang, H.; Liang, Y.; Gong, M.; Li, Y.; Chang, W.; Mefford, T.; Zhou, J.; Wang, J.; Regier, T.; Wei, F.; Dai, H. An Ultrafast Nickel-iron Battery from Strongly Coupled Inorganic Nanoparticle/Nanocarbon Hybrid Materials. *Nat. Commun.* **2012**, *3*, 917.
- (6) Hang, B. T.; Thang, D. H.; Nga, N. T.; Minh, P. T. L.; Kobayashi, E. Nanoparticle Fe₂O₃-Loaded Carbon Nanofibers as Iron-Air Battery Anodes. *J. Electrochem. Soc.* **2013**, *160* (9), A1442–A1445.
- (7) Wang, Z. Y.; Liu, C. J. Preparation and Application of Iron Oxide/Graphene Based Composites for Electrochemical Energy Storage and Energy Conversion Devices: Current Status and Perspective. *Nano Energy* **2015**, *11*, 277–293.
- (8) Ku, J. H.; Jung, Y. S.; Lee, K. T.; Kim, C. H.; Oh, S. M. Thermoelectrochemically Activated MoO₂ Powder Electrode for Lithium Secondary Batteries. *J. Electrochem. Soc.* **2009**, *156* (8), A688–A693.
- (9) Luo, L. L.; Wu, J. S.; Xu, J. M.; Dravid, V. P. Atomic Resolution Study of Reversible Conversion Reaction in Metal Oxide Electrodes for Lithium-Ion Battery. *ACS Nano* **2014**, *8* (11), 11560–11566.
- (10) Minakshi, M.; Singh, P.; Carter, M.; Prince, K. The Zn-MnO₂ battery: The Influence of Aqueous LiOH and KOH Electrolytes on the Intercalation Mechanism. *Electrochem. Solid-State Lett.* **2008**, *11* (8), A145–A149.
- (11) Pan, H.; Shao, Y.; Yan, P.; Cheng, Y.; Han, K. S.; Nie, Z.; Wang, C.; Yang, J.; Li, X.; Bhattacharya, P.; Mueller, K. T.; Liu, J. Reversible Aqueous Zinc/Manganese Oxide Energy Storage from Conversion Reactions. *Nat. Energy* **2016**, *1*, 16039.
- (12) Wang, H. W.; Hu, Z. A.; Chang, Y. Q.; Chen, Y. L.; Lei, Z. Q.; Zhang, Z. Y.; Yang, Y. Y. Facile Solvothermal Synthesis of a Graphene Nanosheet-bismuth Oxide Composite and its Electrochemical Characteristics. *Electrochim. Acta* **2010**, *55* (28), 8974–8980.
- (13) Gujar, T. P.; Shinde, V. R.; Lokhande, C. D.; Han, S. H. Electrosynthesis of Bi₂O₃ Thin Films and their Use in Electrochemical Supercapacitors. *J. Power Sources* **2006**, *161* (2), 1479–1485.
- (14) Liu, Y.; Ying, Y. L.; Mao, Y. Y.; Gu, L.; Wang, Y. W.; Peng, X. S. CuO Nanosheets/rGO Hybrid Lamellar Films with Enhanced Capacitance. *Nanoscale* **2013**, *5* (19), 9134–9140.
- (15) Augustyn, V.; Come, J.; Lowe, M. A.; Kim, J. W.; Taberna, P. L.; Tolbert, S. H.; Abruña, H. D.; Simon, P.; Dunn, B. High-rate Electrochemical Energy Storage through Li⁺ Intercalation Pseudocapacitance. *Nat. Mater.* **2013**, *12* (6), 518–522.
- (16) Yan, X. Y.; Fray, D. J. Electrochemical Studies on Reduction of Solid Nb₂O₅ in Molten CaCl₂-NaCl Eutectic. *J. Electrochem. Soc.* **2005**, *152* (10), E308–E318.
- (17) Monteiro, J. F.; Ivanova, Y. A.; Kovalevsky, A. V.; Ivanou, D. K.; Frade, J. R. Reduction of Magnetite to Metallic Iron in Strong Alkaline Medium. *Electrochim. Acta* **2016**, *193*, 284–292.
- (18) Zhao, X.; Wang, H. E.; Cao, J.; Cai, W.; Sui, J. H. Amorphous/Crystalline Hybrid MoO₂ Nanosheets for High-energy Lithium-ion Capacitors. *Chem. Commun.* **2017**, *53* (77), 10723–10726.
- (19) Qian, Y. X.; Niehoff, P.; Zhou, D.; Adam, R.; Mikhailova, D.; Pyschik, M.; Borner, M.; Klopsch, R.; Rafaja, D.; Schumacher, G.; Ehrenberg, H.; Winter, M.; Schappacher, F. Investigation of Nano-sized Cu(II)O as a High Capacity Conversion Material for Li-metal Cells and Lithium-ion Full Cells. *J. Mater. Chem. A* **2017**, *5* (14), 6556–6568.
- (20) Yao, Z. P.; Kim, S.; Aykol, M.; Li, Q. Q.; Wu, J. S.; He, J. G.; Wolverton, C. Revealing the Conversion Mechanism of Transition Metal Oxide Electrodes during Lithiation from First-Principles. *Chem. Mater.* **2017**, *29* (21), 9011–9022.
- (21) Lee, S. Y.; Wu, L. J.; Poyraz, A. S.; Huang, J. P.; Marschilok, A. C.; Takeuchi, K. J.; Takeuchi, E. S.; Kim, M.; Zhu, Y. M. Lithiation Mechanism of Tunnel-Structured MnO₂ Electrode Investigated by in Situ Transmission Electron Microscopy. *Adv. Mater.* **2017**, *29* (43), 1703186.
- (22) Sato, N.; Kudo, K.; Noda, T. Single Layer of the Passive Film on Fe. *Corros. Sci.* **1970**, *10*, 785–794.
- (23) Schmuki, P.; Virtanen, S.; Davenport, A. J.; Vitus, C. M. In situ X-ray Absorption Near-edge Spectroscopic Study of the Cathodic Reduction of Artificial Iron Oxide Passive Films. *J. Electrochem. Soc.* **1996**, *143* (2), 574–582.
- (24) Huo, G.; Lu, X.; Huang, Y.; Li, W.; Liang, G. Electrochemical Performance of Fe₂O₃ Particles as Anode Material for Aqueous Rechargeable Batteries. *J. Electrochem. Soc.* **2014**, *161* (6), A1144–A1148.
- (25) Kitamura, H.; Zhao, L.; Hang, B. T.; Okada, S.; Yamaki, J.-i. Effect of Charge Current Density on Electrochemical Performance of Fe/C Electrodes in Alkaline Solutions. *J. Electrochem. Soc.* **2012**, *159* (6), A720–A724.
- (26) Allanore, A.; Lavelaine, H.; Valentin, G.; Birat, J. P.; Lapique, F. Iron Metal Production by Bulk Electrolysis of Iron Ore Particles in Aqueous Media. *J. Electrochem. Soc.* **2008**, *155* (9), E125–E129.
- (27) Allanore, A.; Lavelaine, H.; Valentin, G.; Birat, J. P.; Delcroix, P.; Lapique, F. Observation and Modeling of the Reduction of Hematite Particles to Metal in Alkaline Solution by Electrolysis. *Electrochim. Acta* **2010**, *55* (12), 4007–4013.
- (28) Liu, J. L.; Chen, M. H.; Zhang, L. L.; Jiang, J.; Yan, J. X.; Huang, Y. Z.; Lin, J. Y.; Fan, H. J.; Shen, Z. X. A Flexible Alkaline Rechargeable Ni/Fe Battery Based on Graphene Foam/Carbon Nanotubes Hybrid Film. *Nano Lett.* **2014**, *14* (12), 7180–7187.
- (29) Allen, P. D.; Hampson, N. A.; Bignold, G. J. The Electro-dissolution of Magnetite. 2. the Oxidation of Bulk Magnetite. *J. Electroanal. Chem. Interfacial Electrochem.* **1980**, *111* (2–3), 223–233.
- (30) He, Z.; Gudavarthy, R. V.; Koza, J. A.; Switzer, J. A. Room-Temperature Electrochemical Reduction of Epitaxial Magnetite Films

to Epitaxial Iron Films. *J. Am. Chem. Soc.* **2011**, *133* (32), 12358–12361.

(31) Nakayama, S.; Kaji, T.; Shibata, M.; Notoya, T.; Osakai, T. Which is Easier to Reduce, Cu_2O or CuO ? *J. Electrochem. Soc.* **2007**, *154* (1), C1–C6.

(32) Deutscher, R. L.; Woods, R. Characterization of Oxide Layers on Copper by Linear Potential Sweep Voltammetry. *J. Appl. Electrochem.* **1986**, *16* (3), 413–421.

(33) Nakayama, S.; Kimura, A.; Shibata, M.; Kuwabata, S.; Osakai, T. Voltammetric Characterization of Oxide Films Formed on Copper in Air. *J. Electrochem. Soc.* **2001**, *148* (11), B467–B472.

(34) Seo, M.; Ishikawa, Y.; Kodaira, M.; Sugimoto, A.; Nakayama, S.; Watanabe, M.; Furuya, S.; Minamitani, R.; Miyata, Y.; Nishikata, A.; Notoya, T. Cathodic Reduction of the Duplex Oxide Films Formed on Copper in Air with High Relative Humidity at 60°C. *Corros. Sci.* **2005**, *47* (8), 2079–2090.

(35) Bailey, M. R.; Donne, S. W. Electrochemical Characterization of Proton Diffusion during Discharge and Cycling of $\gamma\text{-MnO}_2$. *J. Electrochem. Soc.* **2013**, *160* (11), A2070–A2077.

(36) Ozolins, V.; Zhou, F.; Asta, M. Ruthenia-Based Electrochemical Supercapacitors: Insights from First-Principles Calculations. *Acc. Chem. Res.* **2013**, *46* (5), 1084–1093.

(37) Browning, G. J.; Donne, S. W. Proton Diffusion in Gamma-manganese Dioxide. *J. Appl. Electrochem.* **2005**, *35* (9), 871–878.

(38) MacArthur, D. M. The Proton Diffusion Coefficient for the Nickel Hydroxide Electrode. *J. Electrochem. Soc.* **1970**, *117*, 729–733.

(39) Liu, B.; Yuan, H. T.; Zhang, Y. S.; Zhou, Z. X.; Song, D. Y. Cyclic Voltammetric Studies of Stabilized Alpha-nickel Hydroxide Electrode. *J. Power Sources* **1999**, *79* (2), 277–280.

(40) Ishikawa, K.; Yoshioka, T.; Sato, T.; Okuwaki, A. Solubility of Hematite in LiOH , NaOH and KOH Solutions. *Hydrometallurgy* **1997**, *45* (1–2), 129–135.

(41) Li, H.; Balaya, P.; Maier, J. Li-storage via Heterogeneous Reaction in Selected Binary Metal Fluorides and Oxides. *J. Electrochem. Soc.* **2004**, *151* (11), A1878–A1885.

(42) Débart, A.; Dupont, L.; Poizot, P.; Leriche, J. B.; Tarascon, J. M. A Transmission Electron Microscopy Study of the Reactivity Mechanism of Tailor-Made CuO Particles toward Lithium. *J. Electrochem. Soc.* **2001**, *148* (11), A1266–A1274.

(43) Moser, F.; Fourgeot, F.; Rouget, R.; Crosnier, O.; Brousse, T. In situ X-ray Diffraction Investigation of Zinc Based Electrode in Ni-Zn Secondary Batteries. *Electrochim. Acta* **2013**, *109*, 110–116.

(44) Simic, N.; Ahlberg, E. Electrochemical, Spectroscopic and Structural Investigations of the $\text{Cd}/\text{Cd(II)}$ System in Alkaline Media. I. Cation Effects. *J. Electroanal. Chem.* **1998**, *451* (1–2), 237–247.

(45) Simic, N.; Ahlberg, E. Electrochemical, Spectroscopic and Structural Investigations of the $\text{Cd}/\text{Cd(II)}$ System in Alkaline Media. 2. Concentration Effects. *J. Electroanal. Chem.* **1999**, *462* (1), 34–42.

(46) Horkans, J.; Shafer, M. W. An Investigation of the Electrochemistry of a Series of Metal Dioxides with Rutile-type Structure: MoO_2 , WO_2 , ReO_2 , RuO_2 , OsO_2 and IrO_2 . *J. Electrochem. Soc.* **1977**, *124*, 1202–1207.

(47) Cheng, Y.; Yan, M. M.; Jiang, Z. Y. Electrochemical Behavior and Reduction Mechanism of High Valence Silver Oxide in Alkaline Solution. *Electrochem. Solid-State Lett.* **2007**, *10* (3), F5–F8.

(48) Ogura, K.; Haruyama, S.; Nagasaki, K. The Electrochemical Oxidation and Reduction of Gold. *J. Electrochem. Soc.* **1971**, *118*, 531–535.

(49) Conway, B. E. Electrochemical Oxide Film Formation at Noble-Metals as a Surface-Chemical Process. *Prog. Surf. Sci.* **1995**, *49* (4), 331–452.

(50) Nakayama, S.; Sugihara, T.; Matsumoto, J.; Notoya, T.; Osakai, T. Chemical State Analysis of Tin Oxide Films by Voltammetric Reduction. *J. Electrochem. Soc.* **2011**, *158* (10), C341–C345.

(51) Birss, V. I.; Chan, M.; Phan, T.; Vanysek, P.; Zhang, A. An Electrochemical Study of the Composition of Thin, Compact Pd Oxide Films. *J. Chem. Soc., Faraday Trans.* **1996**, *92* (20), 4041–4047.

(52) Pourbaix, M. *Atlas of Electrochemical Equilibria in Aqueous Solutions*; National Association of Corrosion Engineers: TX, 1966.

(53) Poizot, P.; Laruelle, S.; Grugeon, S.; Dupont, L.; Tarascon, J. M. Nano-sized Transition-metaloxides as Negative-electrode Materials for Lithium-ion Batteries. *Nature* **2000**, *407* (6803), 496–499.

(54) Tu, W. Y.; Liu, W. J.; Cha, C. S.; Wu, B. L. Study of the Powder/Membrane Interface by using the Powder Microelectrode Technique I. The Pt-black/Nafion (R) Interfaces. *Electrochim. Acta* **1998**, *43* (24), 3731–3739.

(55) Sopčič, S.; Peter, R.; Petravič, M.; Mandić, Z. New Insights into the Mechanism of Pseudocapacitance Deterioration in Electrodeposited MnO_2 under Negative Potentials. *J. Power Sources* **2013**, *240*, 252–257.

(56) Xiao, L. A.; Lu, J. T.; Liu, P. F.; Zhuang, L. Determination of Ionic Conductivity and its Impact on Proton Diffusion Model for Nickel Hydroxide. *J. Phys. Chem. B* **2006**, *110* (5), 2057–2063.

(57) Castle, E.; Surman, P. L. Self-diffusion of Oxygen in Magnetite. Techniques for Sampling and Isotopic Analysis of Micro Quantities of Water. *J. Phys. Chem.* **1967**, *71*, 4255–4259.